Dalton Transactions

ROYAL SOCIETY OF CHEMISTRY

PAPER

View Article Online
View Journal

Check for updates

Cite this: DOI: 10.1039/d5dt00960j

Engineering the composition of $Sn_{1-x}Mn_xS$ solid solution nanoparticles for sustainable energy storage†

J. Delphin, [a] M. Daniel Sweetlin*[a] and D. S. Ivan Jebakumar *[b]

Received 23rd April 2025,
Accepted 16th July 2025

DOI: 10.1039/d5dt00960j

rsc.li/dalton

Driven by the growing need for cost-effective and efficient energy storage devices, numerous efforts have been devoted to the sustainable design and development of electrode materials. To meet this demand, we propose tin sulfide–manganese sulfide solid solution nanoparticle-based electrodes as a viable solution, operating in conjunction with a cytocompatible phosphate-buffered saline solution as the electrolyte. In this study, the $Sn_{1-x}Mn_xS$ solid solution nanoparticles of three different compositions were synthesized using a wet chemical route. After investigating the structural, microstructural, and dielectric properties, the electrochemical performance of the electrode as a function of manganese concentration was evaluated to determine the optimal composition of the solid solution for electrochemical energy storage. Our results highlight the significant potential of tin sulfide–manganese sulfide solid solution nanoparticles at a 20 at% manganese concentration as the optimal composition, which can achieve a specific capacitance of 47.6 mF cm^{-2} at a current density of 0.05 mA cm^{-2} and show excellent capacitance retention over 2000 cycles with no observable performance degradation.

Published on 28 July 2025. Downloaded by Yunnan University on 8/6/2025 1:05:53 PM.

1. Introduction

The demand for efficient energy storage materials has garnered significant research attention in recent years, aiming to address renewable energy intermittency and to drive global decarbonization efforts.[1] Electrochemical energy storage (EES) devices play a key role in decarbonizing electricity, further demonstrating their versatility and robustness across a wide range of applications, from transportation to bioelectronics.[1,2]

In response to this need, batteries and supercapacitors (SCs) have emerged as the most mature and reliable technologies for high-performance energy storage applications.[3] In the past few decades, there has been an increasing focus on developing strategies to enhance the performance of energy storage devices, primarily guided by the principles of eco-design, while ensuring operation in biocompatible electrolytes and maintaining safety standards.[3,4] In the present context, phosphate-buffered saline (1× PBS, pH 7.4), a green electrolyte known for its excellent biocompatibility and reasonable ionic conductivity, has emerged as an ideal candidate[5] for sustainable energy storage applications. In this regard, a few studies[6,7] have demonstrated biocompatible supercapacitors by leveraging the unique advantages of phosphate-buffered saline.

Among tin chalcogenides, tin(II) sulfide has been demonstrated to be an effective electrode material, utilizing sodium sulfate as an electrolyte for energy storage applications.[8] Nevertheless, the electrochemical performance of tin(II) sulfide-based supercapacitors is limited by its inherently low specific capacitance and other performance constraints. To overcome these limitations, recent efforts have demonstrated that doping tin sulfide with up to 9% manganese significantly enhances the energy storage capabilities, though these improvements have primarily been observed in strong alkaline electrolytes.[9] However, to render SnS-based supercapacitors suitable for bioelectronic applications, it is essential to investigate their energy storage performance in bio-compatible electrolytes. In this context, the present work aims to extend previous findings by synthesizing a substitutional solid solution of tin sulfide with manganese, systematically varying the manganese concentration, and identifying the optimal concentration level for enhanced electrochemical performance in a bio-compatible PBS electrolyte. The integration of the PBS electrolyte with the SnS–MnS system may represent a significant step toward the development of eco-friendly energy storage technologies.[3]

Given these considerations, we endeavour to optimize the composition of $Sn_{1-x}Mn_xS$ solid solution nanoparticles for use as a positive electrode in supercapacitor-based energy storage

[a]Department of Physics and Research Centre, St John's College, (Affiliated to Manonmaniam Sundaranar University, Abishekapatti, Tirunelveli), Tirunelveli-627002, Tamil Nadu, India. E-mail: danielsweetlin@gmail.com
[b]Department of Chemistry, St John's College, Tirunelveli-627002, Tamil Nadu, India. E-mail: ivanjebakumar@gmail.com

† Electronic supplementary information (ESI) available. See DOI: https://doi.org/10.1039/d5dt00960j

Published on 28 July 2025. Downloaded by Yunnan University on 8/6/2025 1:05:53 PM.

systems assisted by a cytocompatible electrolyte. Therefore, the present study adopts a material design approach aimed at enhancing the electrochemical performance of the electrode, thereby contributing towards the development of more efficient, bio-compatible and environmentally friendly energy storage systems.

2. Materials and methods

2.1. Materials

All chemicals employed in the synthesis were purchased from commercial sources and used without further purification. Stannous chloride dihydrate ($SnCl_2{\cdot}2H_2O$, 98% purity, Loba Chemie), sodium sulfide ($Na_2S{\cdot}xH_2O$, 60% purity, Loba Chemie), manganese chloride tetrahydrate ($MnCl_2{\cdot}4H_2O$, 98% purity, Loba Chemie), ethanol (C_2H_5OH, 99.9%, Generic), and deionized water were used.

2.2. Synthesis of $Sn_{1-x}Mn_xS$ solid solution nanoparticles

$Sn_{1-x}Mn_xS$ solid solution nanoparticles with Mn atomic concentrations of 10%, 20%, and 30% were synthesized using a modified wet chemical technique[10] reported in the literature. In a typical synthesis, 50 mL of an aqueous solution containing an appropriate amount of manganese chloride tetrahydrate ($MnCl_2{\cdot}4H_2O$) and 0.1 M tin chloride dihydrate ($SnCl_2{\cdot}2H_2O$) was prepared using deionized water, mixed and stirred at 1000 rpm for 1 h. Subsequently, 50 mL of 0.2 M Na_2S aqueous solution was added dropwise to the stirred mixture, and the resulting suspension was stirred for 15 minutes. The colour of the resulting suspension gradually changed from brown to brownish-black as the manganese concentration was increased. The temperature of the reaction mixture was then increased to 313 K and maintained at this temperature for 2 h under vigorous stirring. The resulting precipitate was centrifuged at 2300 rpm and washed several times with deionised water and ethanol to remove unreacted reactants and impurities. The collected precipitate was then annealed at 343 K in a hot air oven for 1 hour to obtain the dried sample, which was stored at room temperature for further characterization.

2.3. Characterization

The powder diffraction patterns of the solid solution nanoparticles were acquired using PANalytical X'Pert PRO PW3040/60 X-ray diffractometer by employing Cu Kα radiation (λ = 1.5406 Å) as the radiation source. The morphological images of the nanoparticles were acquired using TESCAN VEGA3 scanning electron microscope, and elemental analysis was performed using the attached energy-dispersive X-ray spectrometer. For dielectric measurements, the samples were pressed using a hydraulic press, resulting in pellets with a diameter of 1.2 cm and a thickness of 1.40 mm. The dielectric measurements were conducted on the pellets using two-probe method over a frequency range of 100 Hz to 200 kHz with Hioki IM3523 LCR meter. The electrochemical energy storage potential of the fabricated electrodes was evaluated by performing electrochemical analyses in a standard three-electrode system by employing CH Instruments CHI660 C electrochemical workstation at room temperature (298 K).

2.4 Electrode fabrication

The energy storage properties of the synthesized sample were evaluated using 1× phosphate-buffered saline (PBS) solution (pH 7.4), which mimics physiological conditions by avoiding toxic or corrosive electrolytes and can be used for low-impact energy storage of portable bio-compatible electronic devices. The working electrode was fabricated by mixing the electroactive material with activated carbon and polytetrafluoroethylene in an 80 : 10 : 10 mass ratio. The mixture was then dispersed in ethanol to form a homogeneous slurry, which was then uniformly applied on a nickel foam within a 1 cm^2 active area and was dried at 343 K for 6 hours to ensure complete solvent evaporation. The mass loading of the prepared electrode was found to be approximately 2 mg cm^{-2}. A platinum wire was used as the auxiliary electrode, while a silver–silver chloride (Ag/AgCl) electrode was used as the reference electrode.

3. Results and discussion

3.1 Structural analysis

Powder X-ray diffraction (XRD) analysis was employed to identify the crystalline phase of the synthesized solid solution nanoparticles. Fig. 1 presents the powder X-ray diffraction patterns obtained for the $Sn_{1-x}Mn_xS$ solid solution nanoparticles at Mn atomic concentrations of 10%, 20%, and 30%. The diffraction peaks observed for all the samples correspond to the orthorhombic phase and are in concordance with the standard data for stannous sulfide (JCPDS card no. 39-0354). In addition, the absence of impurity peaks related to manganese-based compounds suggests that Mn^{2+} ions are effectively substituted into

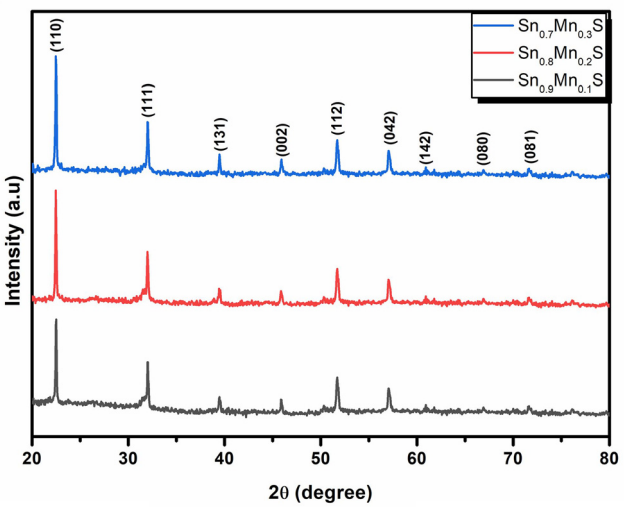

Fig. 1 Powder diffractograms of $Sn_{1-x}Mn_xS$ solid solution nanoparticles.

This journal is © The Royal Society of Chemistry 2025

Published on 28 July 2025. Downloaded by Yunnan University on 8/6/2025 1:05:53 PM.

the SnS crystal lattice to form a solid solution. The diffraction patterns of the solid solution nanoparticles indicate that the intensity of the diffraction peaks increases with a decrease in the full width at half maximum (FWHM) as the concentration of Mn increases in the host lattice. This observation signifies an increase in crystallinity and crystallite size with the incorporation of manganese in the host lattice.

The average crystallite size (D) of the prepared nanoparticles was calculated using the Scherrer equation:

$$D = \frac{K\lambda}{\beta(2\theta)\cos\theta} \quad (1)$$

where λ is the X-ray wavelength (1.5406 Å), β is the full width at half maximum (FWHM) of the diffraction peaks (in radians) and θ is the Bragg angle. The average crystallite size was found to be 28 nm at a 10 at% Mn concentration and gradually increased to 33 nm at a 30 at% Mn concentration (Table 1). The comparable ionic radii of Mn^{2+} (0.80 Å) and Sn^{2+} (1.02 Å) facilitate effective substitution of Mn^{2+} into the SnS lattice.[11]

Table 1 Calculated lattice parameters, cell volume and average crystallite size of solid solution nanoparticles

Sample	Lattice parameters			Unit cell volume (Å^3)	Average crystallite size D (nm)
	a (Å)	b (Å)	c (Å)		
$Sn_{0.9}Mn_{0.1}S$	4.179	10.975	3.977	182.460	28
$Sn_{0.8}Mn_{0.2}S$	4.175	10.987	3.976	182.462	31
$Sn_{0.7}Mn_{0.3}S$	4.180	10.981	3.975	182.500	33

3.2 Microstructural analysis

Scanning electron microscopy (SEM) was performed to analyse the surface morphology of the as-synthesized solid solution nanoparticles. Fig. 2(a–c) displays panoramic views of the $Sn_{0.9}Mn_{0.1}S$, $Sn_{0.8}Mn_{0.2}S$ and $Sn_{0.7}Mn_{0.3}S$ solid solution nanoparticles. The corresponding magnified SEM images shown in Fig. 2(d–f) reveal that the nanoparticles predominantly exhibit a roughly cubic morphology, with the particle size ranging between 175 and 325 nm.

The surface elemental composition of the synthesized samples was analysed using energy-dispersive X-ray spectroscopy (EDS) to confirm the successful incorporation of Mn^{2+} into the host lattice of tin(II) sulfide. The EDS spectra of the $Sn_{0.9}Mn_{0.1}S$, $Sn_{0.8}Mn_{0.2}S$ and $Sn_{0.7}Mn_{0.3}S$ solid solution nanoparticles, shown in Fig. S1–S3,† reveal the presence of tin, manganese, and sulfur in all samples, along with a negligible amount of chlorine. The surface elemental composition of the solid solution nanoparticles is listed in Table 2. In particular, it should be noted that the manganese content increases from $Sn_{0.9}Mn_{0.1}S$ to $Sn_{0.7}Mn_{0.3}S$, although it does not align with the theoretical value.

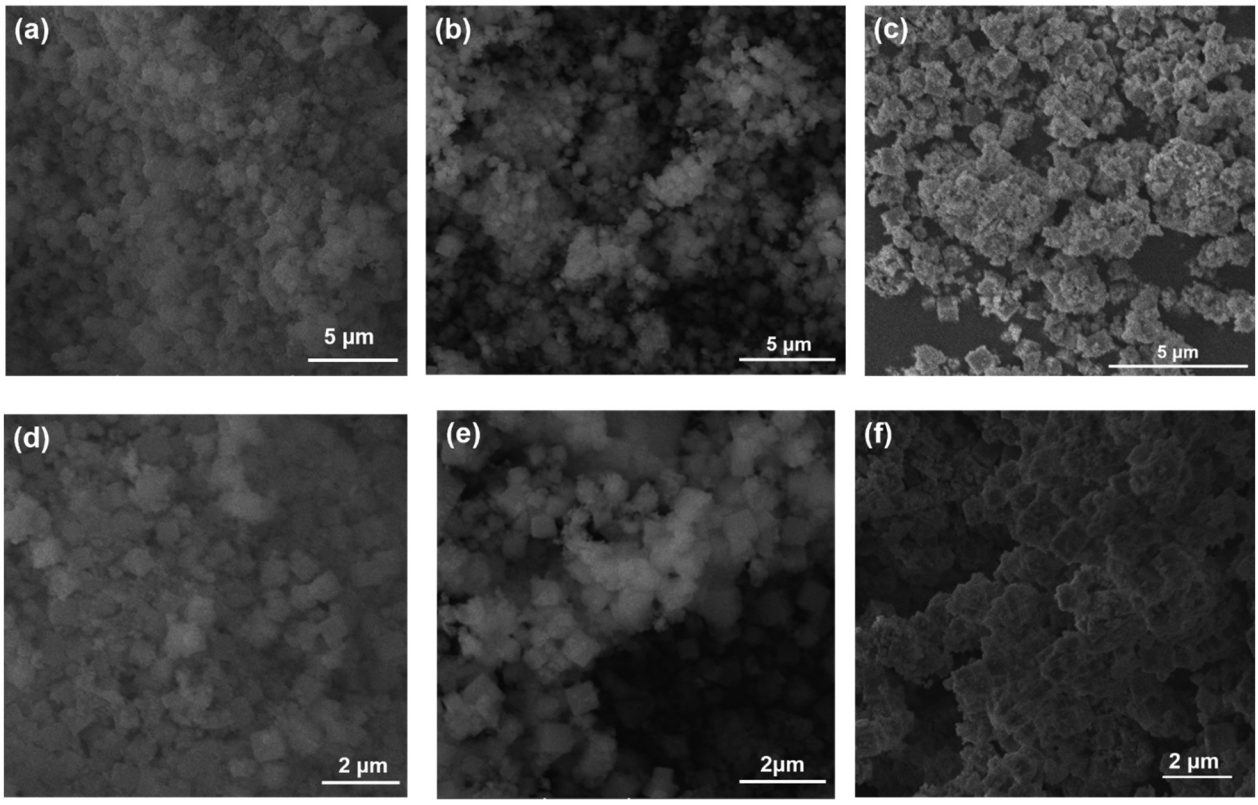

Fig. 2 Low and high magnification scanning electron micrographs of the solid solution nanoparticles: (a) and (d) $Sn_{0.9}Mn_{0.1}S$; (b) and (e) $Sn_{0.8}Mn_{0.2}S$; (c) and (f) $Sn_{0.7}Mn_{0.3}S$.

Published on 28 July 2025. Downloaded by Yunnan University on 8/6/2025 1:05:53 PM.

Table 2 Elemental composition of $Sn_{1-x}Mn_xS$ solid solution nanoparticles

Element (wt %)	Sn	S	Mn	Cl
$Sn_{0.9}Mn_{0.1}S$	73.22	21.87	4.08	0.83
$Sn_{0.8}Mn_{0.2}S$	68.44	22.80	8.00	0.76
$Sn_{0.7}Mn_{0.3}S$	62.83	24.52	12.14	0.51

3.3 Electrical analysis

3.3.1 Dielectric constant and loss tangent. The investigation of dielectric properties is a crucial aspect in assessing the suitability of materials for energy storage, particularly regarding the contribution from the electric dipoles present in the electrostatic double layer.[12]

In this study, the dielectric properties of $Sn_{1-x}Mn_xS$ solid solution nanoparticles were analyzed as a function of frequency at room temperature. The dielectric constant of the prepared nanoparticles in the pellet form is estimated using the following formula:[13]

$$\varepsilon_r = \frac{Cd}{\varepsilon_0 A} \quad (2)$$

where C is the measured capacitance, d is the thickness of the pellet, A is the area of the pellet, and ε_0 is the permittivity of free space (8.85×10^{-12} F m^{-1}). The variation of the dielectric constant (ε) with frequency is shown in Fig. 3(a) for all the compositions of the solid solutions. The dielectric constant shows a sharp decline in the low-frequency region, followed by stabilization at higher frequencies. It is clear that the dielectric constant increases with the increasing manganese concentration across the entire frequency range, reaching its highest value for the sample with the greatest Mn content. Similarly, the variation of loss tangent with frequency for the solid solutions of different compositions at room temperature is presented in Fig. 3(b). It could be observed that the dielectric loss decreases with increasing frequency, which could be due to the loss of contribution from space charge polarization.[9] Moreover, it is observed that dielectric loss decreases with an increase in frequency, reaching a minimum in high-frequency region.

3.3.2 AC conductivity. The AC conductivity of a dielectric sample can be calculated using the relation:[13]

$$\sigma_{ac} = \varepsilon_r \varepsilon_0 \omega \tan \delta \quad (3)$$

where ε_r is the relative dielectric constant, ε_0 is the permittivity of free space (8.85×10^{-12} F m^{-1}), and ω is the angular frequency. The alternating current (AC) conductivity of $Sn_{1-x}Mn_xS$ solid solution nanoparticles, as depicted in Fig. 4, exhibits a frequency-dependent response at room temperature.

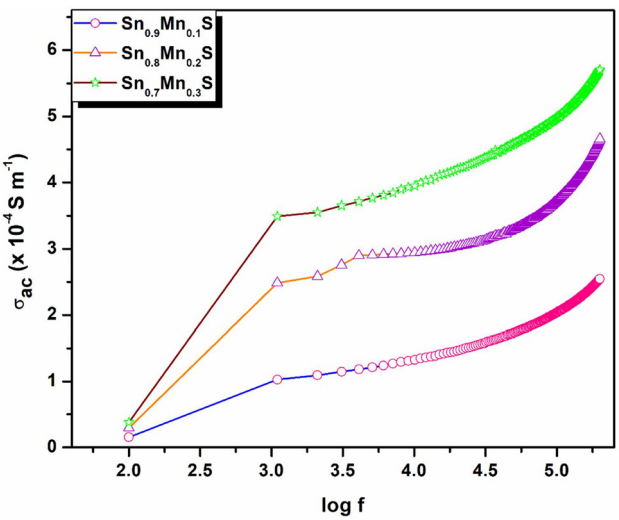

Fig. 4 Variation of AC conductivity with frequency for different compositions.

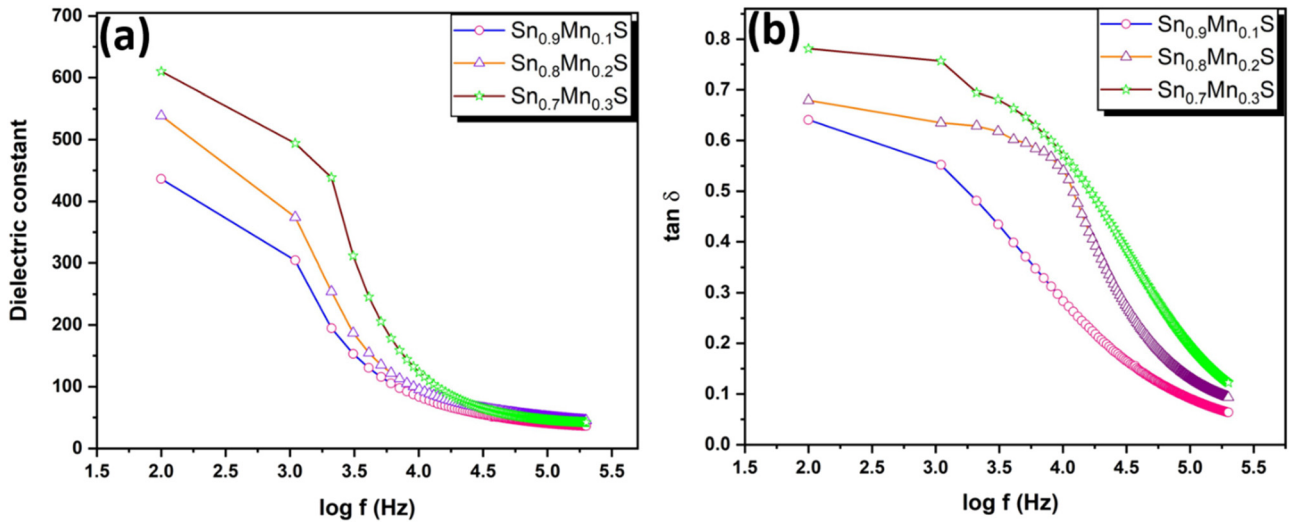

Fig. 3 (a) Dielectric constant and (b) loss tangent as a function of frequency for different compositions of the solid solutions.

This journal is © The Royal Society of Chemistry 2025

Published on 28 July 2025. Downloaded by Yunnan University on 8/6/2025 1:05:53 PM.

3.4 Electrochemical analysis

3.4.1 Cyclic voltammetric (CV) analysis. Cyclic voltammetry (CV) was employed to investigate the nature of charge storage mechanisms in the prepared solid solutions. The cyclic voltammetry response from the electrodes fabricated from solid solution nanoparticles was recorded at scan rates ranging from 5 to 200 mV s^{-1} within the potential window of 0.0–0.5 V *vs.* Ag/AgCl using phosphate-buffered saline (PBS) as the electrolyte. The observed traces shown in Fig. 5(a–c) exhibit a quasi-rectangular profile, a characteristic of pseudocapacitive behaviour,[14] within the measured electrochemical window. The blunt and slanted nature of the observed CV profiles, deviating from the ideal rectangular shape, is attributed to the presence of series and parallel resistive elements within the system.[14]

The absence of sharp redox peaks corresponding to any of the manganese ion species further supports the dominance of a surface-limited redox-based pseudocapacitive energy storage mechanism in the prepared solid solutions. The solid solution nanoparticles with the lowest Mn concentration ($Sn_{0.9}Mn_{0.1}S$) exhibited good electrochemical performance at all scan rates, except at 200 mV s^{-1}. In contrast, the $Sn_{0.8}Mn_{0.2}S$ and $Sn_{0.7}Mn_{0.3}S$ solid solution nanoparticles exhibited excellent electrochemical performance at all the sweep rates. It is important to note that the area enclosed by the CV curve of the $Sn_{0.8}Mn_{0.2}S$ solid solution nanoparticles is slightly higher than those of the other two compositions, indicating their superior electrochemical performance. For reference, the cyclic voltammetric responses of the activated carbon-based electrode (Sigma-Aldrich), fabricated and tested under identical conditions, are provided (Fig. S4†) in the supplementary information.

3.4.2 Electrochemical impedance (EI) analysis. Electrochemical impedance analysis (EIA) provides valuable insights into the electrode–electrolyte interface of the various electrode samples fabricated from solid solution nanoparticles. The measurements were conducted at the open circuit potential over the frequency range of 0.01–100 kHz using PBS as the electrolyte (pH = 7.4) by applying a constant perturbation potential of 5 mV. To provide key insights into the electrochemical behavior of the samples, the Nyquist plot is graphed and presented in Fig. 5(d). The response obtained from the electrode corresponds to that of a non-ideal capacitor with low resistance.[14]

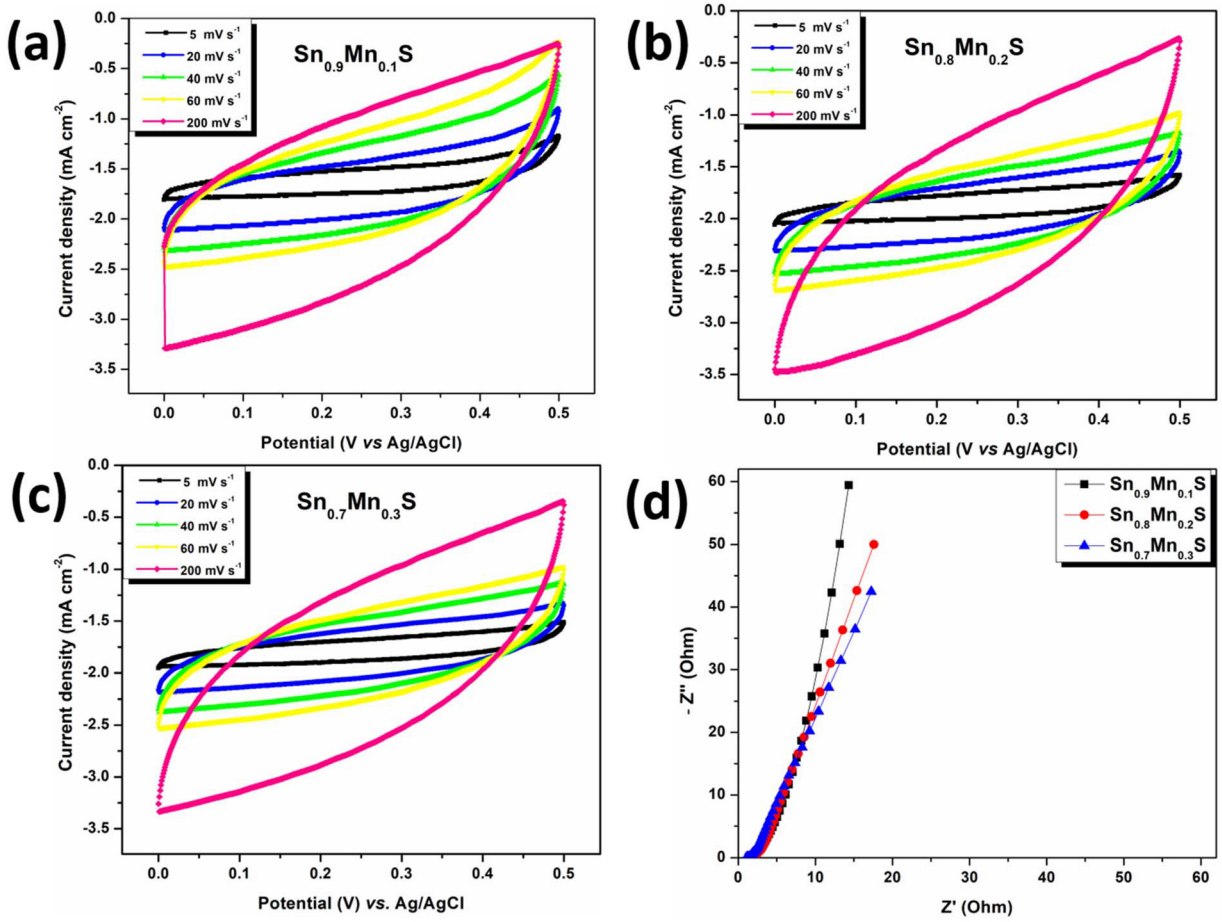

Fig. 5 Cyclic voltammetry (CV) response from (a) $Sn_{0.9}Mn_{0.1}S$, (b) $Sn_{0.8}Mn_{0.2}S$ and (c) $Sn_{0.7}Mn_{0.3}S$ solid solutions at different scan rates. (d) Nyquist plot of $Sn_{1-x}Mn_xS$ solid solution nanoparticles.

Published on 28 July 2025. Downloaded by Yunnan University on 8/6/2025 1:05:53 PM.

In the low-frequency region, the imaginary part of the complex impedance, which is inversely proportional to capacitance, decreases with increasing Mn^{2+} concentration in the SnS lattice, although it exhibits a transition toward non-ideal capacitive behaviour. However, the real part of the impedance, which signifies resistance, decreases as the manganese content in the host lattice increases. Consequently, the solid solution $Sn_{0.8}Mn_{0.2}S$ nanoparticles, characterized by notably low resistance and high capacitance, are considered the optimized composition for energy storage applications.

3.4.3 Galvanostatic charge–discharge (GCD) analysis. Galvanostatic charge–discharge (GCD) experiments were conducted in a 1× PBS electrolyte within the potential range of 0–0.5 V *vs.* Ag/AgCl electrode in order to investigate the charge–discharge characteristics. The GCD response from the electrodes fabricated from different solid solutions for various current densities ranging from 0.05 to 1 mA cm^{-2}, shown in Fig. 6(a–c), displays the characteristics of a pseudocapacitor.[15] The absence of plateau features in the voltage response confirms the absence of bulk diffusion-limited faradaic reactions within the measured potential range. The areal specific capacitance (C_{sp}) of the solid solution nanoparticles is determined from the discharge time using the equation:

$$C_{sp} = \frac{I\Delta t_d}{A\Delta V} \quad (4)$$

where (I) represents the charging/discharging current (A), Δt_d is the discharge time (s), A denotes the active area of the device (cm^2), and ΔV corresponds to the potential window (V).

The specific capacitance values calculated from the GCD curves of the investigated samples at various current densities (0.05–1 mA cm^{-2}) are plotted in Fig. 6(d). It can be observed that the specific capacitance tends to decrease with increasing current densities for all the samples. It was observed that the $Sn_{0.8}Mn_{0.2}S$ solid solution-based electrode demonstrated better electrochemical performance compared to other compositions, achieving the highest areal specific capacitance of 47.6 mF cm^{-2} at a current density of 0.05 mA cm^{-2}.

It is evident that the increase in pseudocapacitance up to the critical concentration ($Sn_{0.8}Mn_{0.2}S$) can be attributed to surface redox reactions[16,17] involving manganese ion species [Mn(II)→ Mn(III) ⇌ Mn(IV)] during the galvanostatic cycling

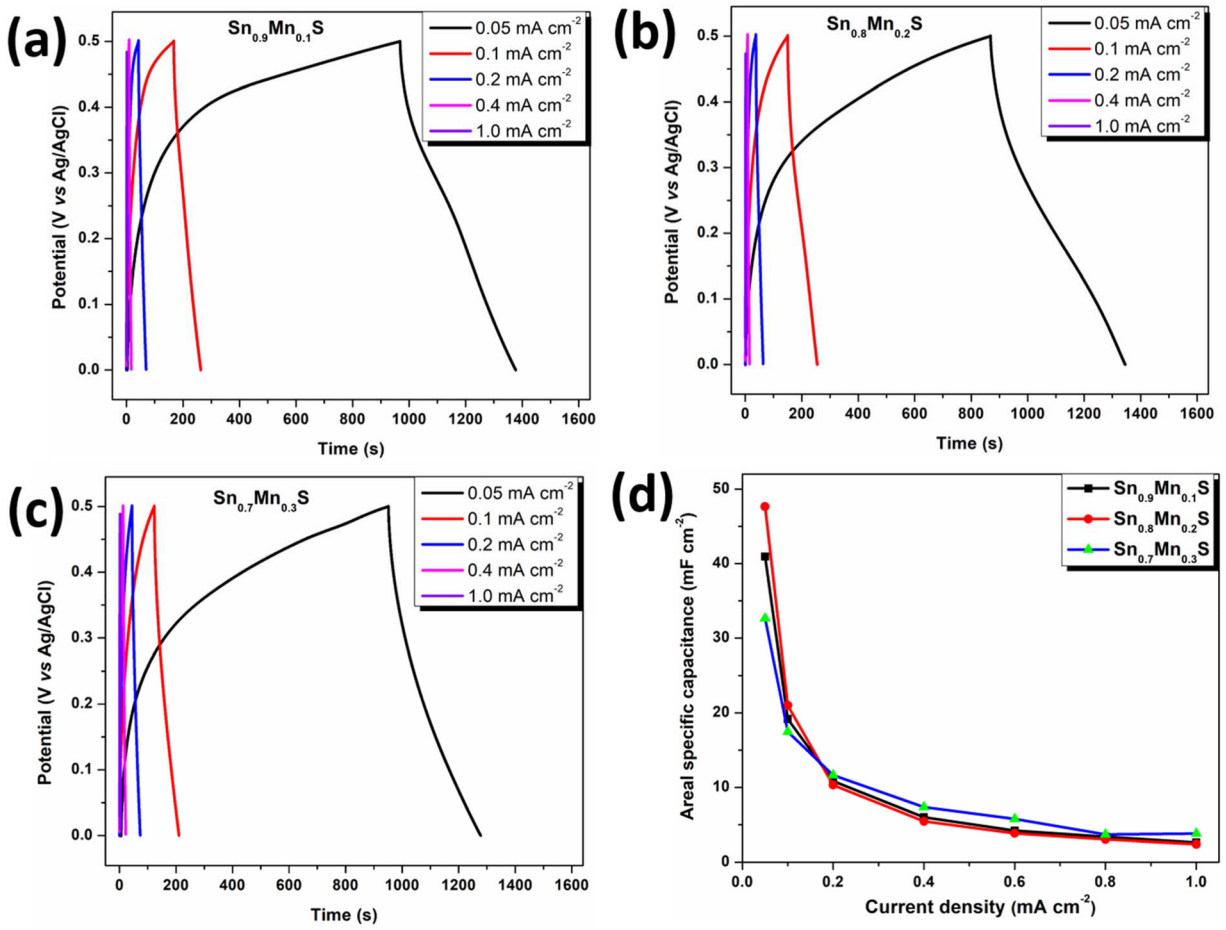

Fig. 6 GCD characteristics of (a) $Sn_{0.9}Mn_{0.1}S$, (b) $Sn_{0.8}Mn_{0.2}S$ and (c) $Sn_{0.7}Mn_{0.3}S$ solid solution nanoparticles. (d) Areal specific capacitance of different solid solution nanoparticles as a function of current density.

 This journal is © The Royal Society of Chemistry 2025

Published on 28 July 2025. Downloaded by Yunnan University on 8/6/2025 1:05:53 PM.

process.[18,19] However, to precisely elucidate the nature and dynamics of these redox processes during cycling, the use of *in operando* techniques is essential.[20] The discharge times for $Sn_{0.9}Mn_{0.1}S$, $Sn_{0.8}Mn_{0.2}S$ and $Sn_{0.7}Mn_{0.3}S$ are 409.2, 476.6 and 326.2 seconds, respectively, at a current density of 0.05 mA cm^{-2}. The solid solution with a higher manganese concentration, $Sn_{0.7}Mn_{0.3}S$, shows a reduction in discharge time, likely due to the formation of point defects resulting from manganese incorporation. Consequently, the increased defect density in $Sn_{0.7}Mn_{0.3}S$ contributes to higher leakage currents and thus results in a shorter discharge time and lower specific capacitance. Hence, it is evident that the $Sn_{0.8}Mn_{0.2}S$ solid solution-based electrode exhibits the most optimal discharge times among the investigated compositions, consistent with the results obtained from the cyclic voltammetry analysis.

To provide initial insights into the performance metrics, the areal energy density (E_d) and areal power density (P_d) were calculated from the areal specific capacitance (C_{sp}). The electrode fabricated with the solid solution $Sn_{0.8}Mn_{0.2}S$ delivers the energy density and power density of 1.65 μW h cm^{-2} and 12.46 μW cm^{-2}, respectively, at a current density of 0.05 mA cm^{-2}. It could be inferred from Table 3 that the solid solution with 20 at% of Mn in the host SnS lattice exhibits superior electrochemical performance among all the investigated systems. It is worth noting that the areal power density reached a maximum value of 250 μW cm^{-2} at a current density value of 1 mA cm^{-2}.

Table 3 Areal specific capacitance, energy density and power density of $Sn_{1-x}Mn_xS$ solid solution nanoparticles at the current density of 0.05 mA cm^{-2}

Solid solution nanoparticles	Areal capacitance (mF cm^{-2})	Energy density (μW h cm^{-2})	Power density (μW cm^{-2})
$Sn_{0.9}Mn_{0.1}S$	40.9	1.42	12.49
$Sn_{0.8}Mn_{0.2}S$	47.6	1.65	12.46
$Sn_{0.7}Mn_{0.3}S$	32.6	1.13	12.47

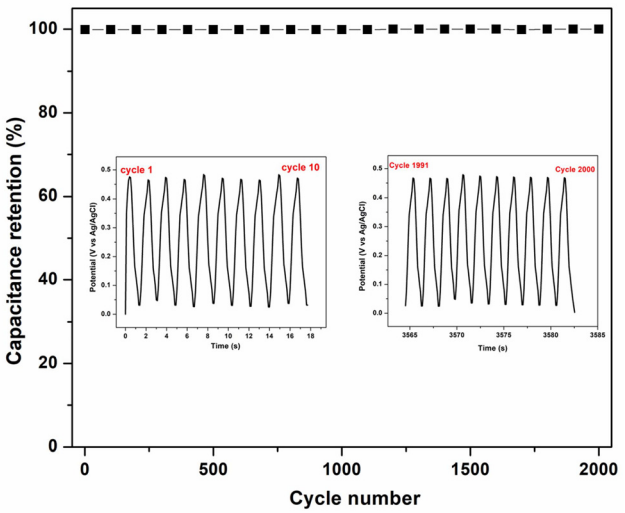

Fig. 7 Cycling stability of the electrode fabricated using $Sn_{0.8}Mn_{0.2}S$ solid solution nanoparticles.

3.4.4 Cycling stability. The cycling stability of the electrode was investigated by measuring the capacitance while reversibly charging and discharging the device for 2000 cycles at a higher current density of 2 mA cm^{-2}. Among all the samples, the $Sn_{0.9}Mn_{0.1}S$ (Fig. S5(a)†) and $Sn_{0.8}Mn_{0.2}S$ (Fig. 7) solid solution nanoparticle-based electrodes exhibited remarkable cycling performance, retaining 100% of their initial areal specific capacitance throughout the test period. On the other hand, the $Sn_{0.7}Mn_{0.3}S$ electrode (Fig. S5(b)†) showed a significant decline in capacitance, retaining only 58% of its initial value after 2000 cycles. It is worth mentioning that the $Sn_{0.8}Mn_{0.2}S$ solid solution-based electrode with appreciable areal specific capacitance preserved the energy storage capability without negligible degradation, maintaining 100% capacitance retention throughout the 2000 cycles.

The electrochemical performance indicators of the solid solution nanoparticle-based electrode ($Sn_{0.8}Mn_{0.2}S$) were found to be consistent with those of the materials previously reported in the literature employing PBS as the green electrolyte, as outlined in Table 4. Finally, the biocompatibility of tin sulfide nanostructures[21] and other Mn-doped nanoparticles[22] is well documented in the literature, suggesting the suitability of the pseudocapacitive electrode material ($Sn_{0.8}Mn_{0.2}S$) for prospective applications in biocompatible energy storage systems. All the findings, including cyclic voltammetry, impedance, and galvanostatic charge–discharge responses, are consistent and underscore the better electrochemical performance of $Sn_{0.8}Mn_{0.2}S$ in terms of specific capacitance, energy density, power density, and extended cycle life for prospective sustainable energy storage.

Table 4 Overview of key electrochemical metrics for selected electrode materials operating in the PBS electrolyte, as documented in the recent literature

Electrode material	Potential window	Electrolyte	Areal specific capacitance	Capacitance retention	Ref.
SnS	0–0.5 V	PBS	44.7 mF cm^{-2} @ 0.3 mA cm^{-2}	100% after 2000 cycles	23
TiN	−0.1–0.6 V	PBS	29.37 mF cm^{-2} @ 0.1 mA cm^{-2}	96% after 10 000 cycles	7
Ti_2N	0.1–0.9 V	PBS	29.36 mF cm^{-2} @ 0.1 mA cm^{-2}	86% after 5000 cycles	24
NbN	−0.1–0.6 V	PBS	13.9 mF cm^{-2} @ 0.2 mA cm^{-2}	92.3% after 10 000 cycles	7
rGO	−0.8 to −0.2 V	PBS	49.84 mF cm^{-2} @ 0.08 mA cm^{-2}	99% after 2000 cycles	25
$Sn_{0.8}Mn_{0.2}S$	0–0.5 V	PBS	47.6 mF cm^{-2} @ 0.05 mA cm^{-2}	100% after 2000 cycles	This work

Published on 28 July 2025. Downloaded by Yunnan University on 8/6/2025 1:05:53 PM.

4. Conclusion

In sum, we have successfully optimized the composition of tin sulfide–manganese sulfide (SnS) solid solution nanoparticles, synthesized using a simple wet chemical method, for sustainable energy storage applications. Powder X-ray diffraction studies revealed that the nanoparticles crystallized in the orthorhombic phase, with average crystallite sizes ranging from 28 to 33 nm. Scanning electron microscopy (SEM) images confirm the cubic morphology of the nanoparticles, with an average particle size of 175–325 nm. The dielectric studies revealed that the dielectric constant and dielectric loss show improvement with increasing concentration of manganese in the solid solution. Electrochemical analyses indicate that the $Sn_{0.8}Mn_{0.2}S$ solid solution is the optimal composition for achieving enhanced electrochemical performance, exhibiting the highest specific capacitance and excellent cycling stability. Overall, the findings of this study demonstrate that incorporating manganese can significantly enhance the energy storage performance of SnS-based electrodes, making them well-suited for sustainable energy storage applications.

Author contributions

J. Delphin: conceptualization, methodology, investigation, formal analysis, writing – original draft; M. Daniel Sweetlin: conceptualization, methodology, supervision, project administration, writing – review and editing; D. S. Ivan Jebakumar: methodology, formal analysis, writing – original draft, supervision, writing – review and editing.

Conflicts of interest

There are no conflicts of interest to declare.

Data availability

The authors declare that the data supporting the findings of this study are available within the paper and included as part of the ESI.†

References

1 H. D. Abruña, Y. Kiya and J. C. Henderson, Batteries and electrochemical capacitors, *Phys. Today*, 2008, **61**(12), 43–47, DOI: **10.1063/1.3047681**.
2 D. Pankratov, Z. Blum and S. Shleev, Hybrid electric power biodevices, *ChemElectroChem*, 2014, **1**, 1798–1807, DOI: **10.1002/celc.201402158**.
3 T. Bertaglia, C. M. Costa, S. Lanceros-Méndez and F. N. Crespilho, Eco-friendly, sustainable, and safe energy storage: A nature-inspired materials paradigm shift, *Mater. Adv.*, 2024, **5**, 7534–7547, DOI: **10.1039/D4MA00363B**.
4 J. S. Chae, N.-S. Heo, C. H. Kwak, W.-S. Cho, G. H. Seol, W.-S. Yoon, H.-K. Kim, D. J. Fray, A. T. Ezhil Vilian, Y.-K. Han, Y. S. Huh and K. C. Roh, A biocompatible implant electrode capable of operating in body fluids for energy storage devices, *Nano Energy*, 2017, **34**, 86–92, DOI: **10.1016/j.nanoen.2017.02.018**.
5 A. R. Kucernak, H. Wang and X. Lin, Avoid using phosphate buffered saline (PBS) as an electrolyte for accurate OER studies, *ACS Energy Lett.*, 2024, **9**, 3939–3946, DOI: **10.1021/acsenergylett.4c01589**.
6 S. He, Y. Hu, J. Wan, Q. Gao, Y. Wang, S. Xie, L. Qiu, C. Wang, G. Zheng, B. Wang and H. Peng, Biocompatible carbon nanotube fibers for implantable supercapacitor, *Carbon*, 2017, **122**, 162–167, DOI: **10.1016/j.carbon.2017.06.053**.
7 S. Sharma, R. Adalati, N. Choudhary, B.S Unnikrishnan, M. Sharma, P. Gopinath and R. Chandra, Physiological fluid based flexible NbN||TiN supercapacitor for biocompatible energy storage applications, *J. Alloys Compd.*, 2023, **960**, 170749, DOI: **10.1016/j.jallcom.2023.170749**.
8 H. Chauhan, M. K. Singh, S. A. Hashmib and S. Deka, Synthesis of surfactant-free SnS nanorods by a solvothermal route with better electrochemical properties towards supercapacitor applications, *RSC Adv.*, 2015, **5**, 17228, DOI: **10.1039/C4RA15563G**.
9 M. A. Dar, S. Dinagaran, D. Govindarajan, S. Rafi Ahamed, F. Habib, C. Siva, A. V. Moholkar, Z. Ahmad and M. A. Yatoo, $Sn_{x-0}Mn_xS$ nanomaterial based electrodes for future-generation supercapacitor and data storage devices, *J. Alloys Compd.*, 2023, **958**, 170523, DOI: **10.1016/j.jallcom.2023.170523**.
10 S. Sohila, M. Rajalakshmi, C. Ghosh, A. K. Arora and C. Muthamizhchelvan, Optical and Raman scattering studies on SnS nanoparticles, *J. Alloys Compd.*, 2011, **509**, 5843, DOI: **10.1016/j.jallcom.2011.02.141**.
11 V. Sidey, On the effective ionic radii for the tin(II) cation, *J. Phys. Chem. Solids.*, 2022, **171**, 110992, DOI: **10.1016/j.jpcs.2022.110992**.
12 A. R. West, *Solid State Chemistry and its Applications*, 2nd edn, John Wiley & Sons, 2007.
13 S. Sagadevan, I. Das, P. Singh and J. Podder, Synthesis of tungsten carbide nanoparticles by hydrothermal method and its characterization, *J. Mater. Sci.:Mater. Electron.*, 2017, **28**, 1136–1141, DOI: **10.1007/s10854-016-5638-3**.
14 T. S. Mathis, N. Kurra, X. Wang, D. Pinto, P. Simon and Y. Gogotsi, Energy storage data reporting in perspective – guidelines for interpreting the performance of electrochemical energy storage systems, *Adv. Energy Mater.*, 2019, **9**(39), 1902007, DOI: **10.1002/aenm.201902007**.
15 Y. Gogotsi and R. M. Penner, Energy storage in nanomaterials – Capacitive, pseudocapacitive, or battery-like?, *ACS Nano*, 2018, **12**(3), 2081–2083, DOI: **10.1021/acsnano.8b01914**.
16 J. P. Zheng and T. R. Jow, A new charge storage mechanism for electrochemical capacitors, *J. Electrochem. Soc.*, 1995, **142**, L6, DOI: **10.1149/1.2043984**.

 This journal is © The Royal Society of Chemistry 2025

Published on 28 July 2025. Downloaded by Yunnan University on 8/6/2025 1:05:53 PM.

17 H. Y. Lee and J. B. Goodenough, Supercapacitor behavior with KCl electrolyte, *J. Solid State Chem.*, 1999, **144**, 220–223, DOI: **10.1006/jssc.1998.8128**.

18 S. Han, S. Park, S.-H. Yi, W. B. Im and S.-E. Chun, Effect of potential and current on electrodeposited MnO_2 as a pseudocapacitor electrode: Surface morphology/chemistry and stability, *J. Alloys Compd.*, 2020, **831**, 154838, DOI: **10.1016/j.jallcom.2020.154838**.

19 H. Jung, M. Taillefert, J. Sun, Q. Wang, O. J. Borkiewicz, P. Liu, L. Yang, S. Chen, H. Chen and Y. Tang, Redox cycling driven transformation of layered manganese oxides to tunnel structures, *J. Am. Chem. Soc.*, 2020, **142**, 2506–2513, DOI: **10.1021/jacs.9b12266**.

20 T. Ramachandran, R. K. Raji, S. Palanisamy, N. Renuka and K. Karuppasamy, The role of in situ and operando techniques in unraveling local electrochemical supercapacitor phenomena, *J. Ind. Eng. Chem.*, 2025, **145**, 144–168, DOI: **10.1016/j.jiec.2024.10.077**.

21 Z. Xie, D. Wang, T. Fan, C. Xing, Z. Li, W. Tao, L. Liu, S. Bao, D. Fana and H. Zhang, Black phosphorus analogue tin sulfide nanosheets: Synthesis and application as near-infrared photothermal agents and drug delivery platforms for cancer therapy, *J. Mater. Chem. B*, 2018, **6**, 4747–4755, DOI: **10.1039/C8TB00729B**.

22 C. Lu, X. Xu, T. Zhang, Z. Wang and Y. Chai, Biocompatible and superparamagnetic manganese-doped iron oxide nanoclusters for diagnostic applications, *ACS Appl. Nano Mater.*, 2022, **5**(2), 2541–2549, DOI: **10.1021/acsanm.1c04201**.

23 J. Delphin, M. Daniel Sweetlin and D. S. Ivan Jebakumar, Cytocompatible electrolyte-assisted pseudocapacitive electrode based on tin monosulfide nanoparticles, *ChemistrySelect*, 2025, **10**, e02542, DOI: **10.1002/slct.202502542**.

24 S. Sharma, R. Adalati, M. Sharma, S. Jindal, A. Kumar, G. Malik and R. Chandra, Single-step fabrication of di-titanium nitride thin-film flexible and biocompatible supercapacitor, *Ceram. Int.*, 2022, **48**(23), 34678–34687, DOI: **10.1016/j.ceramint.2022.08.055**.

25 R. S. Dey, H. A. Hjuler and Q. Chi, Approaching the theoretical capacitance of graphene through copper foam integrated three-dimensional graphene networks, *J. Mater. Chem. A*, 2015, **3**, 6324–6329, DOI: **10.1039/C5TA01112D**.